Heterogeneous interface engineered atomic configuration on ultrathin Ni(OH)$_2$/Ni$_3$S$_2$ nanoforests for efficient water splitting

Qiucheng Xu, Hao Jiang*, Haoxuan Zhang, Yanjie Hu, Chunzhong Li*

Key Laboratory for Ultrafine Materials of Ministry of Education, School of Materials Science and Engineering, East China University of Science & Technology, Shanghai 200237, China

ABSTRACT

The sluggish water dissociation kinetics of low-cost Ni$_3$S$_2$ electrocatalysts severely hinders the hydrogen evolution reaction (HER), resulting in unsatisfied overall water splitting in alkaline media. Herein, we demonstrate the self-assembly of a new nanoforest electrocatalyst by ultrathin Ni(OH)$_2$/Ni$_3$S$_2$ heterogeneous nanosheets (~1.8 nm) using a high-temperature and large-potential electrodeposition technique. The surface atomic configuration of Ni$_3$S$_2$ is well-modulated by hetero-interface engineering with the Ni(OH)$_2$ cocatalyst, effectively accelerating the Volmer step and OH$^-$ adsorption during the HER without sacrificing the oxygen evolution reaction (OER). The resultant electrocatalysts exhibit superior and stable electrocatalytic activity toward the HER and OER in 1 M KOH with small overpotentials of 50 mV and 210 mV at 10 mA cm^{-2}, respectively. Using the Ni(OH)$_2$/Ni$_3$S$_2$ nanoforest as dual-functional electrocatalysts, an alkaline electrolyzer can render 100 mA cm^{-2} at a very low cell voltage of 1.64 V while keep stable for 120 h at 1.55 V, which outperforms the best report for Ni-based electrocatalysts. This finding gives a new insight into the modulating surface atomic configuration for achieving highly active electrocatalysts for water splitting.

1. Introduction

Electrochemical water splitting can convert surplus electrical energy into hydrogen energy, enabling the sustainable utilization of clean energy [1–3]. The efficiency is mainly determined by the hydrogen evolution reaction (HER) and the oxygen evolution reaction (OER) [4–6]. Noble metal Pt and RuO$_2$ can greatly reduce their respective reaction overpotential. However, the development and large-scale application are greatly limited due to their single function and low abundance [7–9]. Low-cost transition metal Ni-based electrocatalysts have recently attracted considerable attention for overall water splitting mainly because of their abundant and active nickel-containing chemical bonds, which are beneficial for realizing surface electrochemical reformation and transformation [10,11]. For example, Ni$_3$S$_2$ has been recognized as an excellent dual-function electrocatalyst theoretically because its rich Ni-S and Ni-Ni bonds not only induce the formation of the more targeted OER intermediate (OOH*) but also facilitate the conversion of the adsorbed hydrogen free radical (H*) into H$_2$ [12,13]. However, the weak OH$^-$ adsorption ability and the sluggish Volmer step-determined water dissociation kinetics (H$_2$O + e$^-$ + * → H* + OH$^-$) of Ni$_3$S$_2$ in alkaline media still result in relatively poor HER performance [14,15].

It is well-known that the catalytic process is a typical surface reaction. The modulation of the surface atomic configuration of Ni$_3$S$_2$ is convenient for balancing the absorption/desorption of the targeted intermediates (OH$^-$ and H*), thereby improving the kinetics of the HER [16,17]. For example, Li et al. [18] deposited Cu nanoparticles on the Ni$_3$S$_2$ surface by a wet chemical reduction method. The density functional theory calculations revealed that the charge accumulation state on Cu, accelerating the water dissociation. Meantime, the rapid electron migration also enhanced the Ni$_3$S$_2$ adsorption to H* intermediates, exhibiting a low overpotential of 128 mV at 10 mA cm^{-2}. On the other hand, it is documented that homogeneous metal-based hybrids possess a more compatible phase potential energy than the heterogeneous metal-based hybrids, which can facilitate the effective modulation of the surface electronic and chemical states of the catalysts [19,20]. Among Ni-based electrocatalysts, the strong adsorption ability of Ni(OH)$_2$ to OH$^-$ can generate substantial H* by water splitting, which can be used as cocatalyst to accelerate the kinetics of the Volmer step-determined water dissociation during the HER for Ni$_3$S$_2$ [21–23]. However, it is a great challenge to reasonably construct the Ni(OH)$_2$/Ni$_3$S$_2$ electrocatalysts to maximize their advantages coupling.

Herein, we demonstrated the rapid synthesis of a new nanoforest electrocatalyst assembled from ultrathin Ni(OH)$_2$/Ni$_3$S$_2$ heterogeneous nanosheets (~ 1.8 nm) by a high-temperature and large-potential

electrodeposition technique. The surface atomic configuration analysis reveals hetero-interface engineering not only decreases the surface work function but also enhances the adsorption to OH^- intermediates, remarkably accelerating the HER kinetics. Furthermore, the loose-knit nanoforest also facilitates the full exposure of active sites and improves electrolyte infiltration and bubble escape. Consequently, the $Ni(OH)_2$/Ni_3S_2 electrocatalysts exhibit superior catalytic activity toward the HER and OER in alkaline media with small overpotentials of 50 mV and 210 mV at 10 mA cm^{-2}, respectively. As dual-functional electrocatalysts, a two-electrode electrolyzer requires only 1.64 V to deliver 100 mA cm^{-2} for overall alkaline water splitting, outperforming the best report for Ni-based electrocatalysts to date. This work provides an insight into the development of efficient dual-functional electrocatalysts by modulating their surface atomic configuration.

2. Experimental

2.1. Preparation

The $Ni(OH)_2$/Ni_3S_2 nanoforest was prepared by one-step electrodeposition in a three-electrode cell using nickel foam (NF, 0.5 cm * 1 cm), a graphite electrode and a saturated Ag/AgCl electrode as the working, counter and reference electrodes, respectively. In a typical process, a voltage of -4.5 V was applied for 120 s in the electrolyte consisting of 3 M $NiCl_2 \cdot 6H_2O$, 7.5 M $CS(NH_2)_2$ and 4 M NaCl at a pH = 2.5 controlled by 1 M H_2SO_4 and a reaction temperature of 65 °C. Then, the targeted $Ni(OH)_2$/Ni_3S_2 nanoforest was obtained by rinsing with deionized water and drying in a vacuum oven at 60 °C for 12 h. For achieving the $Ni(OH)_2$ and Ni_3S_2 nanoforests, the electrolyte was replaced by 3 M $NiCl_2 \cdot 6H_2O$, 4 M NaCl with the pH = 6 and 3 M $NiCl_2 \cdot 6H_2O$, 15 M $CS(NH_2)_2$, 4 M NaCl at a pH = 1.5, respectively. The mass loading of the active materials on nickel foam was calculated by the mass difference before and after the electrodeposition. A typical mass loading was approximately 4.8 mg cm^{-2}.

2.2. Characterization

The structure and morphology of the as-obtained products were characterized by X-ray powder diffraction (XRD; Rigaku D/Max 2550, Cu Ka radiation) at a scan rate of 1° min^{-1}, field emission scanning electron microscopy (FESEM, Hitachi, S-4800, 10 kV) and transmission electron microscopy (FETEM, JEOL, JEM-2100 F) with an X-ray energy dispersive spectrometer (EDS) at an accelerating voltage of 200 kV. A

Scanning Probe Microscope (Veeco, DI) was used to detect the thickness of the samples. X-ray photoelectron spectroscopy (XPS) and the ultraviolet photoemission spectroscopy (UPS) were recorded with a Thermo Scientific ESCALAB 250Xi and a VG Scienta R4000 analyzer (monochromatic He I light source of 21.2 eV), respectively. Raman measurements were performed at room temperature using a Via + RefLex Raman spectrometer with an excitation wavelength of 514 nm. Thermogravimetric analysis (NETZSCH STA409PC) was performed at a heating rate of 10 °C min^{-1} under flowing nitrogen.

Electrochemical measurements were performed in 1 M KOH (pH = 14) using a three electrode system with the as-prepared electrodes, saturated Ag/AgCl electrode and graphite electrode as the working, reference and counter electrodes, respectively. For the powder samples (20 wt% Pt/C or RuO_2), 5 mg of the powder, 0.4 mL of distilled water, 0.52 mL of ethanol and 80 μL of a Nafion solution (5 wt%) were mixed and then drop-coated onto the nickel foam with a mass loading of ~ 2 mg cm^{-2}. The electrocatalytic activities for the HER and OER were measured by using linear sweep voltammetry (LSV) with a scanning rate of 1 mV s^{-1} controlled by a CHI 660E electrochemical workstation (CH Instruments, Inc., Shanghai, China). Electrochemical impedance spectroscopy (EIS) measurements in a frequency range from 0.01 Hz to 100 KHz were performed at an overpotential of 100 mV by an Autolab PGSTAT302 N electrochemical workstation. Double-layer capacitance measurements were made by taking cycle-voltage measurements at a scan rate that ranged from 20 to 100 mV s^{-1}. The turnover frequency (TOF) values of the catalysts were calculated from the equation: TOF = $(J \times A)/(2 \times F \times n)$, where J is the current density at a given overpotential, A is the surface area, F is the Faraday constant (96485 C mol^{-1}), and n is the mole number of the active metal sites for the catalyst deposited on the electrode. For overall water splitting, the as-prepared electrodes were integrated as the anode and the cathode in a two-electrode cell. All potentials measured were calibrated to a reversible hydrogen electrode (RHE) by the following equation: E(RHE) = E(Ag/AgCl) + 0.1976 V + 0.0591 × pH, and all data in electrochemical measurements were 95% iR-corrected with respect to the ohmic resistance of the solution. The solution resistance (R) was calculated based on the EIS results measured at -0.12 V $vs.$ RHE for HER and 1.52 V $vs.$ RHE for OER in frequencies range from 10 kHz to 100 mHz. The resistance value is equal to the total impedance at the phase angle of 0° in high frequency.
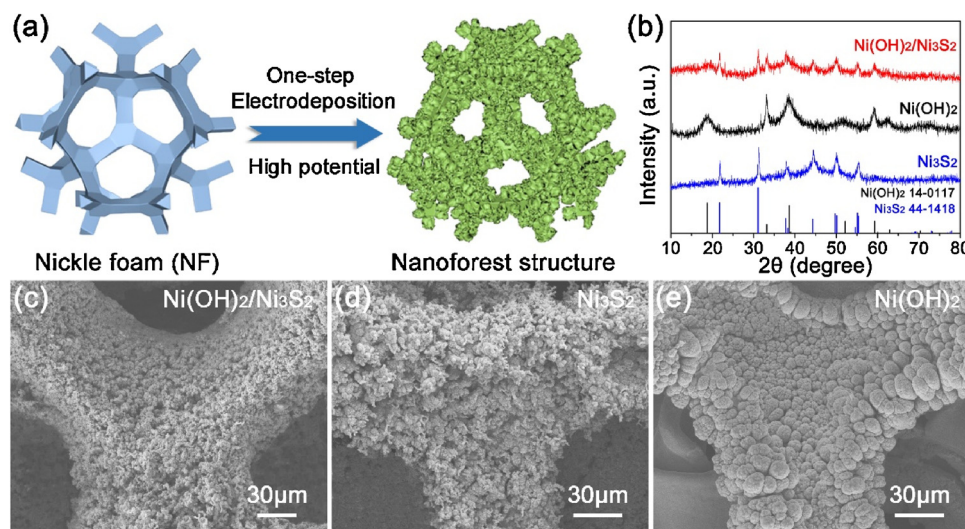

Fig. 1. (a) Schematic illustration of the electrodeposition synthesis of the nanoforest electrocatalysts, (b) XRD patterns of the $Ni(OH)_2$/Ni_3S_2, the $Ni(OH)_2$ and the Ni_3S_2, (c–e) the low-magnification SEM images of the $Ni(OH)_2$/Ni_3S_2, the Ni_3S_2 and the $Ni(OH)_2$ nanoforests, respectively.

3. Results and discussion

3.1. Synthesis and characterizations of Ni(OH)$_2$/Ni$_3$S$_2$ nanoforests

The schematic illustration of the electrodeposition synthesis of the nanoforest electrocatalysts on the NF substrates is illustrated in Fig. 1a. In a typical process, the nanoforest electrocatalysts were formed by applying a consistent high negative potential of -4.5 V (*vs.* saturated Ag/AgCl) at an electrolyte temperature of 65 °C. By changing the electrolyte composition and pH value, the Ni(OH)$_2$-Ni$_3$S$_2$, the Ni(OH)$_2$ and the Ni$_3$S$_2$ nanoforests were prepared separately. For example, the electrolyte for preparing the Ni(OH)$_2$/Ni$_3$S$_2$ nanoforest consisted of nickel dichloride, thiourea and sodium chloride at a pH value of 2.5. The nickel dichloride and thiourea served as the nickel source and sulfur source, respectively. The pH value regulated by 1.0 M H$_2$SO$_4$ was used to control the formation of Ni(OH)$_2$. More details for preparing the Ni$_3$S$_2$ and the Ni(OH)$_2$ nanoforests are given in the experimental section.

The corresponding XRD patterns of the Ni(OH)$_2$/Ni$_3$S$_2$, the Ni(OH)$_2$ and the Ni$_3$S$_2$ are shown in Fig. 1b, where all diffraction peaks can be easily indexed to the Ni$_3$S$_2$ (JCPDS: 44-1418) and the Ni(OH)$_2$ (JCPDS: 14-0117). The results indicate that the Ni(OH)$_2$/Ni$_3$S$_2$ displays the combined characteristic peaks of Ni(OH)$_2$ and Ni$_3$S$_2$, indicating the formation of a composite. The Ni$_3$S$_2$ content in the Ni(OH)$_2$/Ni$_3$S$_2$ is estimated to 45 wt% according to the TG results (**Fig. S1**). Typical SEM images of the Ni(OH)$_2$/Ni$_3$S$_2$, the Ni$_3$S$_2$ and the Ni(OH)$_2$ nanoforests are shown in Fig. 1c–e and **Fig. S2**. The Ni(OH)$_2$/Ni$_3$S$_2$ electrocatalyst demonstrates an integrated nanoforest structure of the Ni$_3$S$_2$ and the Ni(OH)$_2$ with abundant porous pathways. Such a distinctive nanoforest structure is formed with the assistance of the cathodic HER reaction. During the high negative potential electrodeposition process, hydrogen vigorously evolves on the surface of the NF substrates forming a hydrogen bubble soft template for constructing the nanoforest structure [24,25]. To further highlight the advantages of high potential electrodeposition, low-magnification SEM images of the Ni(OH)$_2$/Ni$_3$S$_2$ materials electrodeposited at a low potential of -0.45 V are shown in **Fig. S3**, where a compact morphology is exhibited. In contrast, a nanoforest structure with plentiful connected pore channels is beneficial for both fast active species transportation and gas bubble escape, which boost the electrochemical reaction kinetics.

To further explore the microstructure of the Ni(OH)$_2$/Ni$_3$S$_2$ nanoforest, high-magnification SEM and TEM images are exhibited. Fig. 2a-b show the ultrathin Ni(OH)$_2$/Ni$_3$S$_2$ nanosheets with thicknesses of ~1.8 nm assembled into nanoparticles, further building the nanoforest structure on the NF structures. The AFM in Fig. 2c also verified that the thicknesses of the Ni(OH)$_2$/Ni$_3$S$_2$ nanosheets are ~ 1.8 ± 0.2, which agrees with the TEM results. More structural information of the ultrathin Ni(OH)$_2$/Ni$_3$S$_2$ heterogeneous nanosheets are shown in Fig. 2d, where three separate domains are observed. Particularly, the lattice fringe spacing of 0.181 nm and 0.238 nm with a dihedral angle of 75° in region I area are assigned to the (211) and (003) planes of hexagonal Ni$_3$S$_2$, respectively. The interlayer spacing of 0.156 nm in region III is attributed to the (110) plane of Ni(OH)$_2$. Region II, which is between regions I and III, can be considered the hetero-interface between Ni(OH)$_2$ and Ni$_3$S$_2$. This result can be supported by the selected area FFT patterns of the three domains since region II displays an overlay of regions I and III. The SAED shown in **Fig. S4** also proves the formation of the Ni(OH)$_2$/Ni$_3$S$_2$ heterostructure. The elemental distributions of the Ni(OH)$_2$/Ni$_3$S$_2$ nanoforest are shown in Fig. 2e, where the Ni, S, O elements are uniformly distributed. Furthermore, the microstructure of the Ni(OH)$_2$ and Ni$_3$S$_2$ nanoforests are shown in **Fig. S5** and **Fig. S6**, respectively, where the nanoforest structure are likewise assembled by the ultrathin nanosheet.

The bonding form of the Ni(OH)$_2$/Ni$_3$S$_2$ is characterized by Raman spectra (Fig. 3a), where two distinct peaks at approximately 325 cm^{-1} and 450 cm^{-1} are assigned to the characteristic peaks of the Ni-S bond in Ni$_3$S$_2$ and the Ni–OH bond in Ni(OH)$_2$, respectively [26,27]. Moreover, UPS and XPS are employed to analyze the surface electronic and chemical states of the Ni(OH)$_2$/Ni$_3$S$_2$ electrocatalyst. Fig. 3b shows the UPS spectra and derived work functions of the Ni(OH)$_2$/Ni$_3$S$_2$, the Ni(OH)$_2$ and the Ni$_3$S$_2$. Clearly, the Ni(OH)$_2$/Ni$_3$S$_2$ has the lowest work function among the three samples, which suggests its faster electron transfer efficiency and higher Fermi level energy. Since the energy levels greatly determine the chemical adsorption ability of the reaction intermediates, the increased Fermi level energy can promote the adsorption of hydrogen atoms on Ni(OH)$_2$/Ni$_3$S$_2$ [28]. Furthermore, the deconvolution of the Ni 2p$_{3/2}$ XPS spectrum for the Ni(OH)$_2$/Ni$_3$S$_2$ and the Ni$_3$S$_2$ is shown in Fig. 3c. The peak at 852.5 eV represents the characteristic peak of Ni° in Ni$_3$S$_2$. The three additional peaks at 855.4, 856.7 and 861.6 eV are attributed to the Ni^{2+}, Ni^{3+} and satellite peaks of the Ni(OH)$_2$/Ni$_3$S$_2$, respectively [29]. Notably, the Ni°, Ni^{2+} and Ni^{3+} peaks exhibit obvious negative shifts compared with those of the Ni$_3$S$_2$. Similarly, the S 2p$_{1/2}$ and S 2p$_{3/2}$ peaks in the XPS S 2p spectrum (Fig. 3d) of the Ni(OH)$_2$/Ni$_3$S$_2$ also show a negative shift of 0.4 eV with respect to that of the Ni$_3$S$_2$. These binding energy negative shifts of the Ni 2p$_{3/2}$ and S 2p peaks indicate an increase in the electron density of the Ni(OH)$_2$/Ni$_3$S$_2$, which is benefit to strength the adsorption ability to H* intermediates [30]. In addition, the increase of S-O characteristic peak at 168.7 eV in the XPS S 2p spectrum implies the generation of a new type of S-O bond in the Ni(OH)$_2$/Ni$_3$S$_2$ hetero-interface instead of the oxidized sulfur functional in Ni$_3$S$_2$. Therefore, the above results suggest the surface atomic configuration of Ni$_3$S$_2$ is well-modulated by hetero-interface engineering of the Ni(OH)$_2$ cocatalyst. The Ni(OH)$_2$/Ni$_3$S$_2$ electrocatalyst possesses a faster electron transfer efficiency and an optimized H* absorption ability, which are vital for enhancing the HER activity of the catalyst.

3.2. Electrochemical activity of Ni(OH)$_2$/Ni$_3$S$_2$ nanoforests

The HER performance of the Ni(OH)$_2$/Ni$_3$S$_2$, the Ni(OH)$_2$ and the Ni$_3$S$_2$ electrocatalysts, along with commercial Pt/C on NF and bare NF were evaluated by a standard three-electrode system in 1.0 M KOH electrolyte. The polarization curve of the Ni(OH)$_2$/Ni$_3$S$_2$ in Fig. 4a demonstrates a very small overpotential of 142 mV at 200 mA cm^{-2}, which is better than the commercial Pt/C electrocatalyst and the other compared samples. Additionally, an ultrahigh current density of 1 A cm^{-2} can be achieved at an overpotential of only 310 mV (**Fig. S7**). The online gas chromatography analysis of the Ni(OH)$_2$/Ni$_3$S$_2$ displays a nearly 100% Faradic efficiency calculated by comparing the generated H$_2$ volumes with theoretical values (**Fig. S8** and **Table S1**). The Tafel plots in Fig. 4b reflect the HER kinetics of the electrocatalysts. The Ni(OH)$_2$/Ni$_3$S$_2$ has a small HER Tafel slope of 49 mV dec^{-1}, which is close to the commercial Pt/C electrocatalyst (43 mV dec^{-1}) but much lower than the Ni(OH)$_2$ (60 mV dec^{-1}) and the Ni$_3$S$_2$ (99 mV dec^{-1}). This result indicates that the Ni(OH)$_2$-Ni$_3$S$_2$ is dominated by the Volmer-Heyrovsky mechanism with fast HER kinetics [31].

As shown in Fig. 4c, the EIS tests are used to examine the electrode kinetics under HER operating conditions [32,33]. The charge-transfer resistance (R$_{ct}$) of the Ni(OH)$_2$/Ni$_3$S$_2$ is approximately 8.4 Ω, much lower than the Ni(OH)$_2$ (16.5 Ω) and the Ni$_3$S$_2$ (24.8 Ω), which further confirms the excellent reaction kinetics of the Ni(OH)$_2$/Ni$_3$S$_2$. Additional ESI data are shown in **Table S2**. To explore the active site number and the intrinsic catalytic activity, the electrochemical double-layer capacitance (C$_{dl}$) and the turnover frequency (TOF) were estimated. Fig. 4d shows the Ni(OH)$_2$/Ni$_3$S$_2$ has a calculated double-layer capacitance value of 13.6 m F cm^{-2}, which is much higher than those of the Ni(OH)$_2$ (10.1 m F cm^{-2}) and the Ni$_3$S$_2$ (9.2 m F cm^{-2}). The corresponding electrochemically active surface area (ECSA) results (**Fig. S9**) also indicate the Ni(OH)$_2$/Ni$_3$S$_2$ possess more rich active sites. The TOF values of the Ni(OH)$_2$/Ni$_3$S$_2$, the Ni(OH)$_2$ and the Ni$_3$S$_2$ at the designated overpotential are shown in Fig. 4e. At an overpotential of 100 mV, the Ni(OH)$_2$/Ni$_3$S$_2$ possesses a TOF value of 12.49 s^{-1}, which is
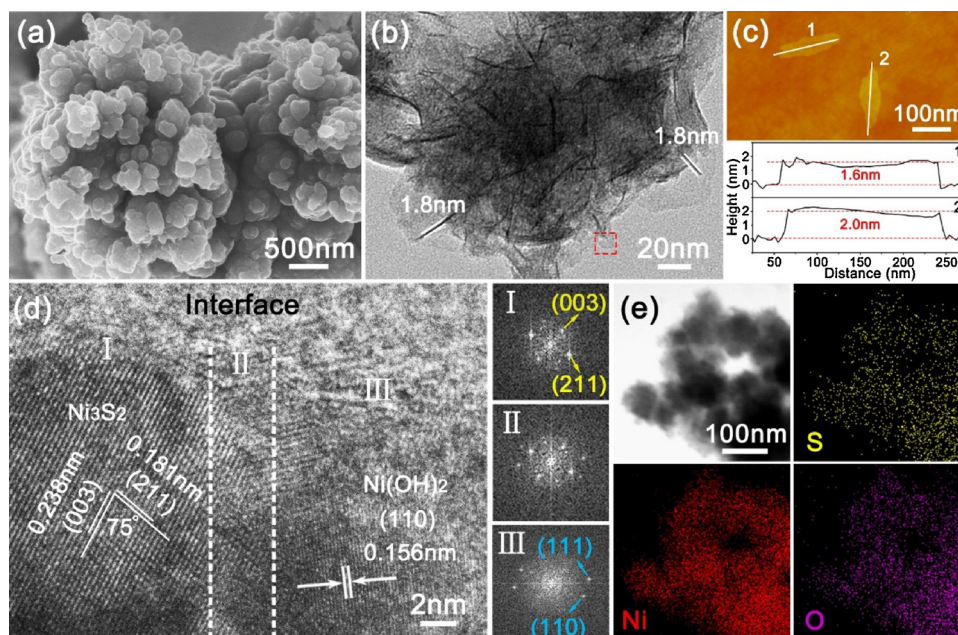
Fig. 2. (a) High-magnification SEM image, (b) low-magnification TEM image, (c) AFM image and the corresponding height profiles, (d) high-resolution TEM image and the selected area FFT patterns, and (e) TEM-EDS mapping of Ni, S, O of the Ni(OH)$_2$/Ni$_3$S$_2$ nanoforest.

two and three times higher than the Ni(OH)$_2$ and the Ni$_3$S$_2$, respectively, exhibiting the best intrinsic HER activity. Fig. 4f exhibits the durability of the Ni(OH)$_2$/Ni$_3$S$_2$ by long-time chronopotentiometry (CP) measurements. After operating at 20 mA cm^{-2} for 240 h, negligible potential degradation and no morphology changes can be found, implying the superior durability for the HER.

Based on the aforementioned discussion, the excellent HER activity of the Ni(OH)$_2$/Ni$_3$S$_2$ electrocatalyst in alkaline media can be mainly ascribed to its hierarchical nanoforest structure and the synergistic effect at the Ni(OH)$_2$/Ni$_3$S$_2$ hetero-interface, as shown in Fig. 5a. Specifically, the nanoforest structure, which is assembled from the ultrathin Ni(OH)$_2$/Ni$_3$S$_2$ heterogeneous nanosheets of ∼1.8 nm, exposes as much

electrocatalytically active sites as possible for the HER. Additionally, the porous structure of the nanoforest on the NF substrate not only fasts electron transfer efficiency but also provides easier gas bubble escape pathways. The comparison of the electrochemical performance of the nanoforest structure and the compact structure of Ni(OH)$_2$/Ni$_3$S$_2$ is exhibited in Fig. S10. It is obvious that the nanoforest structure sample shows better HER activity and a larger ECSA. Moreover, the synergistic catalytic mechanism at the Ni(OH)$_2$/Ni$_3$S$_2$ hetero-interface is explained as follows. It has been mentioned that water dissociation is the rate-determined step for an alkaline HER. For an individual Ni$_3$S$_2$ electrocatalyst, the OH$^-$ adsorption ability is too weak to cleave the HO-H bonds for generating H* intermediates, so that the subsequent H*
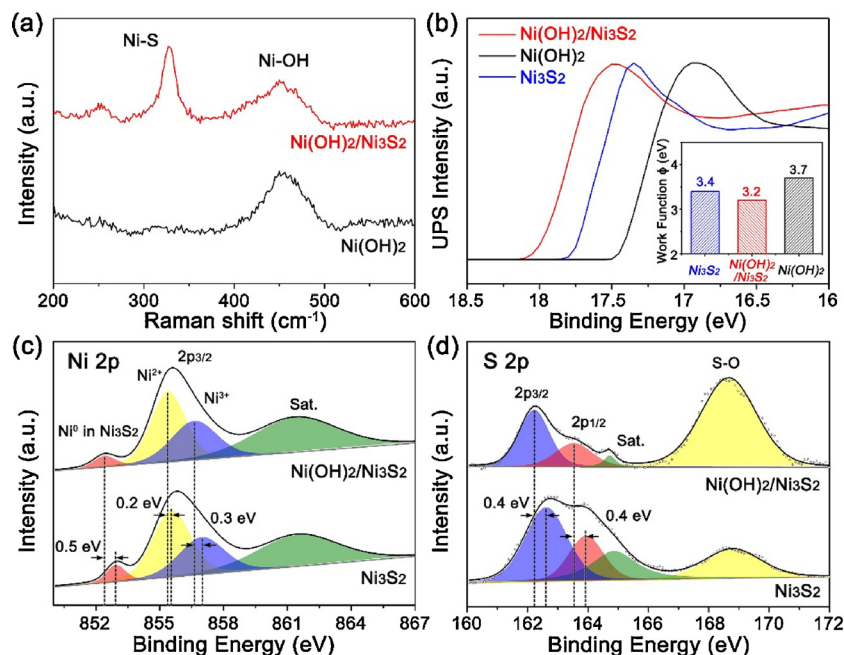

Fig. 3. (a) Raman spectra of the Ni(OH)$_2$/Ni$_3$S$_2$ and the Ni$_3$S$_2$, (b) UPS analysis of the Ni(OH)$_2$/Ni$_3$S$_2$, the Ni(OH)$_2$ and the Ni$_3$S$_2$. High-resolution XPS spectra of (c) Ni 2p and (d) S 2p for the Ni(OH)$_2$/Ni$_3$S$_2$ and the Ni$_3$S$_2$.
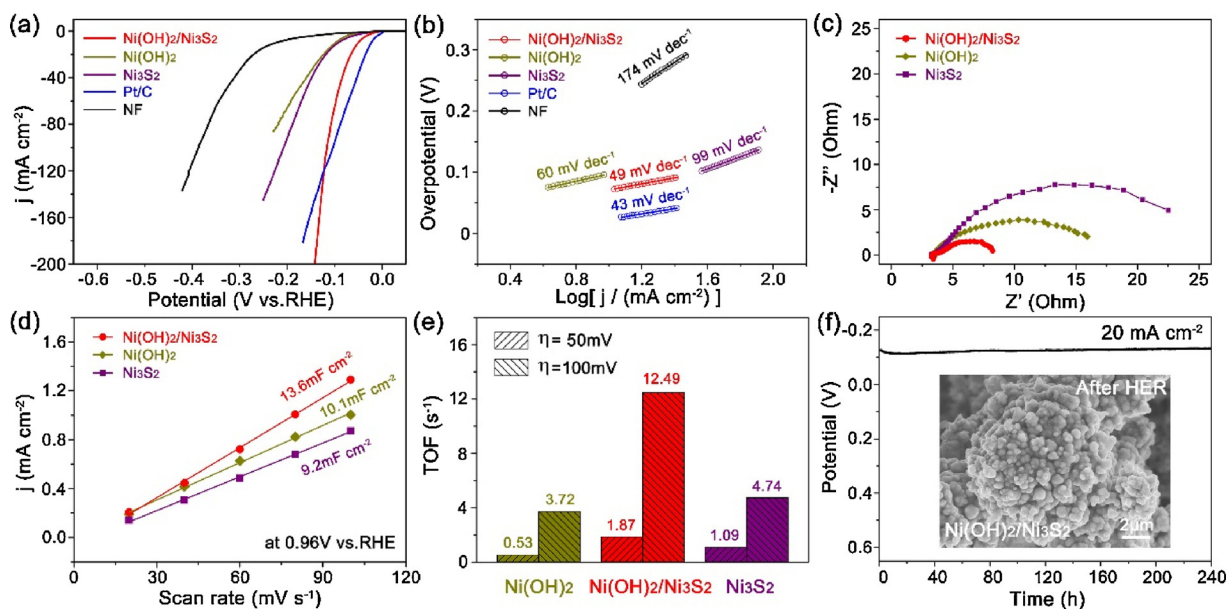
Fig. 4. (a) The HER polarization curves and (b) Tafel plots of the Ni(OH)$_2$/Ni$_3$S$_2$, the Ni(OH)$_2$, the Ni$_3$S$_2$, NF and commercial Pt/C electrocatalysts. (c) Nyquist plots, (d) electrochemical double-layer capacitance (C$_{dl}$) and (e) turnover frequency of the Ni(OH)$_2$/Ni$_3$S$_2$, the Ni(OH)$_2$, the Ni$_3$S$_2$. (f) Stability tests of the Ni(OH)$_2$/Ni$_3$S$_2$ by CP measurements at 20 mA cm^{-2}. The inset shows the SEM image after 240 h of the HER.

intermediate recombination step is severely impeded [18,34]. With the assistance of the Ni(OH)$_2$ cocatalyst, H$_2$O molecules can be effectively dissociated into H* and OH$^-$ intermediates at the Ni(OH)$_2$ side owing to its strong OH$^-$ adsorption ability [21–23,35]. Then, the produced H* intermediates tend to absorb on the nearby Ni$_3$S$_2$ side and are further recombined into H$_2$ molecules due to the low hydrogen production barrier of Ni$_3$S$_2$. Consequently, the synergistic effect at the Ni(OH)$_2$/ Ni$_3$S$_2$ hetero-interface greatly enhances the HER kinetics, which was verified by the Tafel and EIS results (Fig. 4b, c). To further verify the above hypothesis, the ex-situ O 1 s XPS spectrum of the Ni(OH)$_2$/Ni$_3$S$_2$ and the Ni$_3$S$_2$ before and after the HER are shown in Fig. 5b–c. Three distinct peaks at 530.9, 531.7 and 532.7 eV correspond to the OH$^-$

functional group or adsorbed OH$^-$ radical, the S-O functional group and the adsorbed H$_2$O, respectively. Evidently, the increasing intensity of the OH$^-$ peak for the Ni(OH)$_2$/Ni$_3$S$_2$ before and after 1 h HER test is 3.64, which is much higher than that of the Ni$_3$S$_2$ nanoforest (1.77). These results indicate that more adsorbed OH$^-$ radicals are formed on the surface of the Ni(OH)$_2$/Ni$_3$S$_2$ electrocatalyst, implying the enhanced OH$^-$ adsorption ability and improved water dissociation kinetics.

The OER performance of the Ni(OH)$_2$/Ni$_3$S$_2$ electrocatalyst was investigated by comparing it with bare NF, the Ni(OH)$_2$, the Ni$_3$S$_2$ and the state-of-the-art RuO$_2$ electrocatalysts. Fig. 6a shows the polarization curve, where the Ni(OH)$_2$/Ni$_3$S$_2$ exhibits an excellent OER activity in accordance with the state-of-the-art RuO$_2$ electrocatalyst. The Ni(OH)$_2$/
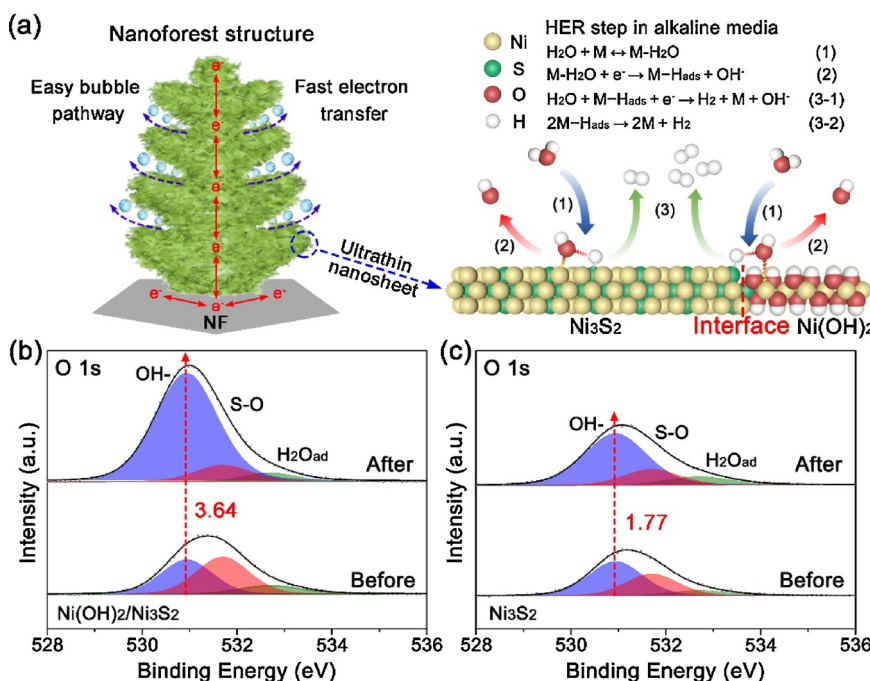

Fig. 5. (a) Schematic illustration of the HER activity enhancing mechanism of the Ni(OH)$_2$/Ni$_3$S$_2$ nanoforest in alkaline media, (b–c) O 1 s XPS spectra of the Ni(OH)$_2$/Ni$_3$S$_2$ and the Ni$_3$S$_2$, respectively, before and after the HER.

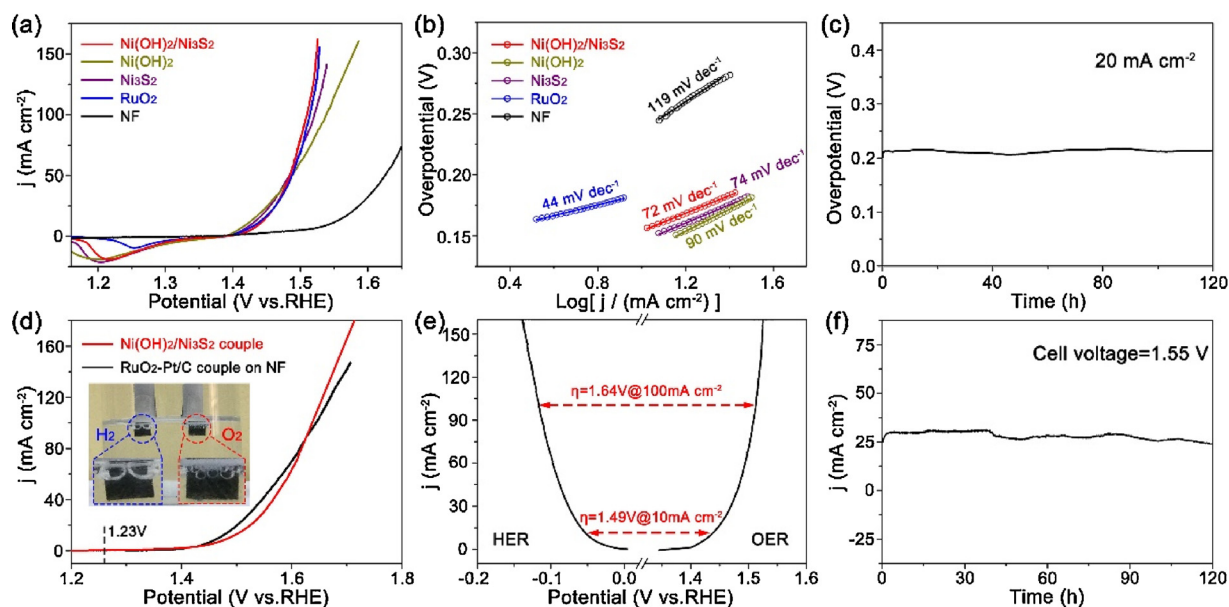**Fig. 6.** (a) The OER polarization curves and (b) Tafel plots of the Ni(OH)$_2$/Ni$_3$S$_2$, the Ni(OH)$_2$, the Ni$_3$S$_2$, bare NF and the state-of-the-art RuO$_2$ electrocatalysts, (c) stability tests of the Ni(OH)$_2$/Ni$_3$S$_2$ by CP measurements at 20 mA cm^{-2}. (d) The overall water splitting polarization curves of the Ni(OH)$_2$/Ni$_3$S$_2$‖Ni(OH)$_2$/Ni$_3$S$_2$ and the Pt/C‖RuO$_2$ electrocatalysts in the two-electrode configuration, (e) the polarization curves showing the dual functionality of the Ni(OH)$_2$/Ni$_3$S$_2$ toward both the HER and OER in a three-electrode configuration, and (f) stability tests of the Ni(OH)$_2$/Ni$_3$S$_2$ nanoforest.

Ni$_3$S$_2$ requires only a small overpotential of 280 mV to reach 100 mA cm^{-2}, which is lower than those of the Ni(OH)$_2$ (308 mV) and the Ni$_3$S$_2$ (290 mV). The Tafel slopes are shown in Fig. 6b. The Tafel slope of Ni(OH)$_2$/Ni$_3$S$_2$ is as small as 72 mV dec^{-1}, which is larger than that of RuO$_2$ but superior to the Ni(OH)$_2$ (90 mV dec^{-1}), the Ni$_3$S$_2$ (74 mV dec^{-1}) and most of the advanced Ni-based OER catalysts reported recently, such as RGO/NiFe-LDH (85 mV dec^{-1}) [36], Ni$_x$Co$_{3-x}$S$_4$/Ni$_3$S$_2$ (95 mV dec^{-1}) [37] and PE-NiMoP$_2$ (90.6 mV dec^{-1}) [38]. The EIS tests are also exhibited in **Fig. S11**, where the Ni(OH)$_2$/Ni$_3$S$_2$ and RuO$_2$ electrocatalysts possess a similar R$_{ct}$ of ∼ 9.5 Ω. This result demonstrates that the Ni(OH)$_2$/Ni$_3$S$_2$ electrocatalysts have low ion and electron resistances [39,40]. The durability test was then performed at a fixed anodic current density of 20 mA cm^{-2} for 120 h with a negligible potential degradation (Fig. 6c), demonstrating excellent long-term durability.

According to the above results, the self-supported Ni(OH)$_2$/Ni$_3$S$_2$ can serve as both cathode and anode for overall water-splitting in the two-electrode configuration. For comparison, the state-of the-art Pt/C and RuO$_2$ electrocatalysts drop-coated on NF are performed in couple as cathode and anode, respectively. The polarization curves in Fig. 6d show the Ni(OH)$_2$/Ni$_3$S$_2$ couple can reach a current densities of 10 mA cm^{-2} at a cell voltage of only 1.49 V, which is better than the other advanced Ni-based bifunctional electrocatalysts. A comprehensive comparison is listed in **Table S3**. For example, Wehrspohn et al. [41] have recently reported a 3D hierarchical heterostructure NiFe LDH@NiCoP/NF bifunctional electrocatalyst, which achieved 10 mA cm^{-2} at a cell voltage of 1.57 V. Additionally, the current densities of Ni(OH)$_2$/Ni$_3$S$_2$ couple can surpass the Pt/C-RuO$_2$ couple at cell voltages greater than 1.63 V. The inset exhibits the H$_2$ and O$_2$ gas bubbles that evolved on the surface of the cathode and anode, respectively. The corresponding Tafel plots of the overall water splitting polarization curves were provided in **Fig. S12**. Furthermore, Fig. 6e shows the combination of the individual HER and OER polarization curves of the Ni(OH)$_2$/Ni$_3$S$_2$ in a three-electrode configuration. According to the calculated equation ($\eta = \eta_{HER} + \eta_{OER}$), the calculated potentials for achieving current densities of 10 and 100 mA cm^{-2} are 1.49 and 1.64 V, which is in a good agreement with the results tested in the two-electrode configuration. This consistency indicates the good accordant and bifunctional characteristic of the Ni(OH)$_2$/Ni$_3$S$_2$ nanoforest electrocatalyst

[42]. Moreover, the durability test is shown in Fig. 6f. The Ni(OH)$_2$/Ni$_3$S$_2$ couple can be maintained at a cell voltage of 1.55 V for 120 h with a small current density degradation of only 2 mA cm^{-2}. The outstanding overall water splitting activity and stability of the Ni(OH)$_2$/Ni$_3$S$_2$ nanoforest indicate its attractive potential for practical applications.

4. Conclusions

In summary, we report a novel nanoforest electrocatalyst assembled from ultrathin Ni(OH)$_2$/Ni$_3$S$_2$ heterogeneous nanosheets with thicknesses of ∼ 1.8 nm by a high-temperature and large-potential electrodeposition technique. The hetero-interface engendered by introducing Ni(OH)$_2$ cocatalyst has modulated the surface atomic configuration of Ni$_3$S$_2$, effectively accelerating the Volmer step and OH$^-$ adsorption during the HER while maintaining excellent OER activity. The loosened and interconnected nanoforest-like architecture also facilitates the full exposure of active sites with enhanced electrolyte infiltration and bubble escape. As a consequence, the as-obtained Ni(OH)$_2$/Ni$_3$S$_2$ electrocatalysts exhibit superior catalytic activity toward HER and OER with very small overpotentials of 50 mV and 210 mV at 10 mA cm^{-2}, respectively. More remarkably, when applied as dual-functional electrocatalysts, a two-electrode electrolyzer requires only 1.64 V to deliver 100 mA cm^{-2} for overall alkaline water splitting, outperforming the best report for Ni-based electrocatalysts to date. This work provides an insight into the development of efficient dual-functional electrocatalysts by modulating their surface atomic configuration.

Appendix A. Supplementary data

Supplementary material related to this article can be found, in the online version, at doi: https://doi.org/10.1016/j.apcatb.2018.09.064.

References

[1] N.S. Lewis, Science 351 (2016) 1920–1929.
[2] Y. Jiao, Y. Zheng, M. Jaroniec, S.Z. Qiao, Chem. Soc. Rev. 44 (2015) 2060–2086.
[3] I. Roger, M.A. Shipman, M.D. Symes, Nat. Rev. Chem. 1 (2017) 0003.
[4] Z.W. Seh, J. Kibsgaard, C.F. Dickens, I.B. Chorkendorff, J.K. Norskov, T.F. Jaramillo, Science 355 (2017) 4998–5010.
[5] H. Zhao, H. Zhang, G. Cui, Y. Dong, G. Wang, P. Jiang, X. Wu, N. Zhao, Appl. Catal. B: Environ. 225 (2018) 284–290.
[6] J.X. Feng, S.Y. Tong, Y.X. Tong, G.R. Li, J. Am. Chem. Soc. 140 (2018) 5118–5126.
[7] C.L. Hu, L. Zhang, Z.J. Zhao, A. Li, J.L. Gong, Adv. Mater. 12 (2018) 1705538.
[8] L. Chen, H. Jiang, H. Jiang, H. Zhang, S. Guo, Y. Hu, C. Li, Adv. Energy Mater. 7 (2017) 1602782.
[9] C.G. Morales-Guio, L. Sterna, X. Hu, Chem. Soc. Rev. 43 (2014) 6555–6569.
[10] Feng L, G. Yu, Y. Wu, G. Li, H. Li, Y. Sun, T. Asefa, W. Chen, X. Zou, J. Am. Chem. Soc. 137 (2015) 14023–14026.
[11] A. Sivanantham, S. Shanmugam, Appl. Catal. B: Environ. 203 (2017) 485–493.
[12] J.J. Lv, J. Zhao, H. Fang, L.P. Jiang, L.L. Li, J. Ma, J.J. Zhu, Small 24 (2017) 1700264.
[13] J. Zhang, T. Wang, D. Pohl, B. Rellinghaus, R. Dong, S. Liu, X. Zhuang, X.L. Feng, Angew. Chem. Int. Ed. 55 (2016) 6702–6707.
[14] T. Kou, T. Smart, B. Yao, I. Chen, D. Thota, Y. Ping, Y. Li, Adv. Energy Mater. 8 (2018) 1703538.
[15] J. Cao, J. Zhou, Y. Zhang, Y. Wang, X. Liu, ACS appl, Mater. Interfaces 10 (2018) 1752–1760.
[16] Y. Zheng, Y. Jiao, A. Vasileff, S.Z. Qiao, Angew. Chem. Int. Ed. 57 (2018) 7568–7579.
[17] D. Strmcnik, P.P. Lopes, B. Genorio, V.R. Stamenkovic, N.M. Markovic, Nano Energy 29 (2016) 29–36.
[18] J.X. Feng, J.Q. Wu, Y.X. Tong, G.R. Li, J. Am. Chem. Soc. 140 (2018) 610–617.
[19] K.S. Pitzer, J. Am. Chem. Soc. 11 (1962) 2025–2028.
[20] W.P. Gao, Z.D. Hood, M.F. Chi, Acc. Chem. Res. 50 (2017) 787–795.
[21] R. Subbaraman, D. Tripkovic, D. Strmcnik, K.C. Chang, M. Uchimura, A.P. Paulikas, V. Stamenkovic, N.M. Markovic, Science 334 (2011) 1256–1260.
[22] R. Subbaraman, D. Tripkovic, K.C. Chang, D. Strmcnik, A.P. Paulikas, P. Hirunsit, M. Chan, J. Greeley, V. Stamenkovic, N.M. Markovic, Nat. Mater. 11 (2012) 550–557.
[23] J. Yan, H. Wu, H. Chen, L. Pang, Y. Zhang, R. Jiang, L. Li, S. Liu, Appl. Catal. B: Environ. 194 (2016) 74–83.
[24] R. Ma, J. Wang, Z. Yang, M. Liu, J. Zhang, L. Jiang, Adv. Mater. 27 (2015) 2384–2389.
[25] T.N. Huan, G. Rousse, S. Zanna, I.T. Lucas, X. Xu, N. Menguy, V. Mougel, M. Fontecave, Angew. Chem. Int. Ed. 56 (2017) 4792–4796.
[26] Z. Cheng, H. Abernathy, M. Liu, J. Phys. Chem. C 111 (2007) 17997–18000.
[27] M.C. Bernard, R. Cortes, M. Keddam, H. Takenouti, P. Bernard, S. Senyarich, J.Power Sources 63 (1996) 247–254.
[28] X. Li, W. Liu, M. Zhang, Y. Zhong, Z. Weng, Y. Mi, Y. Zhou, M. Li, J.J. Cha, Z. Tang, H. Jiang, X. Li, H.L. Wang, Nano Lett. 17 (2017) 2057–2063.
[29] P. Chen, T. Zhou, M. Zhang, Y. Tong, C. Zhong, N. Zhang, L. Zhang, C. Wu, Y. Xie, Adv. Mater. 30 (2017) 1701584.
[30] H. Zhang, H. Jiang, Y. Hu, P. Saha, C.Z. Li, Mater. Chem. Front. (2018), https://doi.org/10.1039/C8QM00178B.
[31] J. Wang, F. Xu, H. Jin, Y. Chen, Y. Wang, Adv. Mater. 29 (2017) 1605838.
[32] Q.C. Xu, H. Jiang, H.X. Zhang, H.B. Jiang, C.Z. Li, Electrochim. Acta 259 (2018) 962–967.
[33] S. Jing, L. Zhang, L. Luo, J. Lu, S. Yin, P.K. Shen, P. Tsiakaras, Appl. Catal. B: Environ. 224 (2018) 533–540.
[34] Y. Qu, M. Yang, J. Chai, Z. Tang, M. Shao, C.T. Kwok, M. Yang, Z. Wang, D. Chua, S. Wang, Z. Lu, H. Pan, ACS Appl. Mater. Interfaces 9 (2017) 5959–5967.
[35] X. Zhang, Y.Y. Liang, Adv. Sci. 2 (2017) 1700644.
[36] X. Zou, Y. Liu, G. Li, Y. Wu, D. Liu, W. Li, H. Li, D. Wang, Y. Zhang, X. Zou, Adv. Mater. 22 (2017) 1700404.
[37] Y. Wu, Y. Liu, G. Li, X. Zou, X. Lian, D. Wang, L. Sun, T. Asef, X. Zou, Nano Energy 35 (2017) 161–170.
[38] X. Wang, H. Chen, Y. Xu, J. Liao, B. Chen, H. Rao, D. Kuang, C. Su, J. Mater. Chem. A 5 (2017) 7191–7199.
[39] J.X. Feng, H. Xu, Y.T. Dong, S.H. Ye, Y.X. Tong, G.R. Li, Adv. Mater. 128 (2016) 3758–3762.
[40] J.X. Feng, S.H. Ye, H. Xu, Y.X. Tong, G.R. Li, Adv. Mater. 28 (2016) 4698–4703.
[41] H. Zhang, X. Li, A. Hähnel, V. Naumann, C. Lin, S. Azimi, S.L. Schweizer, A.W. Maijenburg, R.B. Wehrspohn, Adv. Funct. Mater. 14 (2018) 1706847.
[42] L. Yang, Z. Guo, J. Huang, Y. Xi, R. Gao, G. Su, W. Wang, L. Cao, B. Dong, Adv. Mater. 46 (2017) 1704574.